J. Fluid Mech. (2010), *vol.* 660, *pp.* 240–257.
doi:10.1017/S0022112010002636

Elliptic instability of a stratified fluid in a rotating cylinder

D. GUIMBARD[1,2], S. LE DIZÈS[1]†, M. LE BARS[1], P. LE GAL[1] AND S. LEBLANC[2]

[1]IRPHE, UMR 6594, CNRS, University of Aix-Marseille, 49 rue F. Joliot Curie, F-13013 Marseille, France

[2]LSEET, UMR 6017, CNRS, University of Toulon-Var, BP 20132, F-83957 La Garde Cedex, France

(Received 14 October 2009; revised 3 May 2010; accepted 3 May 2010; first published online 16 July 2010)

In this paper, we analyse the characteristics of the elliptic instability in a finite cylinder in the presence of both background rotation and axial stratification. A general formula for the linear growth rate of the stationary sinuous modes is derived including viscous and detuning effects in the limit of small eccentricity. This formula is discussed and compared to experimental results which are obtained in a cylinder filled with salted water for two different eccentricities by varying the stratification, the background rotation and the cylinder rotation. A good agreement with the theory concerning the domain of instability of the sinuous modes is demonstrated. Other elliptic instability modes, oscillating at the cylinder angular frequency are also evidenced together with a new type of instability mode, which could be connected to a centrifugal instability occurring during the experimental phase of spin-up. The nonlinear regime of the elliptic instability is also documented. In contrast with the homogeneous case, no cycle involving growth, breakdown and re-laminarization is observed in the presence of strong stratification. The elliptic instability in a stratified fluid seems to yield either a persistent turbulent state or a weakly nonlinear regime.

Key words: stratified flows, vortex instability, waves in rotating fluids

1. Introduction

Vortices in the atmosphere and in the ocean are subjected to both Coriolis and buoyancy forces. The goal of the present paper is to analyse the effect of these forces on the so-called elliptic instability of the vortices. Both theoretical and experimental results are obtained by considering the simple geometry of the flow in a rotating cylinder.

The elliptic instability is a three-dimensional generic instability which occurs when a vortex is subjected to a strain field (see Kerswell 2002, for a review). It appears as a secondary instability in shear flows (Bayly, Orszag & Herbert 1988) and wakes (Leweke & Williamson 1998) and is often associated with their three-dimensional transition to turbulence.

It is also expected to be present in geophysical flows. In the atmosphere, vortex streets can be observed behind isolated islands (Etling 1989) and small-scale vortices are also often created during the baroclinic instability (Polavarapu & Peltier 1993;

† Email address for correspondence: ledizes@irphe.univ-mrs.fr

Lesieur, Métais & Garnier 2000). In the presence of stratification and rotation, these coherent structures can be unstable by different types of instabilities. However, Stegner, Pichon & Beunier (2005) have argued that the cyclone–anticyclone asymmetry of wakes could be associated with an effect of the background rotation on the elliptic instability. The mechanism of the elliptic instability has been discussed in numerous papers (see Kerswell 2002). It is now well established that it is associated with a resonance of vortex modes with a background strain field. Malkus (1989) was the first to recognize that the main ingredients of the instability (rotation + strain) could be reproduced in a controlled way in a laboratory experiment by considering a rotating flow in an elliptically deformed cylinder. This flow configuration has been the subject of numerous experimental works which have been compared to the theory (Malkus 1989; Waleffe 1989; Eloy, Le Gal & Le Dizès 2000, 2003). In contrast with the local approach (Bayly 1986; Lifschitz & Hameiri 1991), the theory in the cylinder takes into account the structure and the dispersion relation of the modes. Explicit formulae can still be obtained for the dominant unstable modes as shown by Waleffe (1989) for the unstratified case. Here, we shall extend these formulae in the presence of stratification and background rotation. Note that Eloy & Le Dizès (2001) and Fukumoto (2003) have demonstrated that theoretical predictions obtained for the cylinder geometry are qualitatively similar for a Rankine vortex. We therefore expect the results obtained in the present paper to apply to vortices with a steep vorticity profile. We shall come back on this point in the final section of the paper.

The analysis of background rotation alone has been previously considered in Le Bars, Le Dizès & Le Gal (2007) for the same geometry. Experiments and theory were compared and a good agreement was demonstrated. Miyazaki & Fukumoto (1992) analysed the effect of axial stratification using a local approach, while Miyazaki (1993) also included Coriolis effects. Kerswell (1993) considered the cylinder geometry without Coriolis effects but also analysed the additional effects of radial stratification and magnetic fields in the perspective of modelling the Earth's outer core. Experimental results have been obtained for vortex pairs in a stratified fluid (Billant, Colette & Chomaz 2004; Cariteau & Flór 2006). However, in this case, the elliptic instability is in competition with the zigzag instability (Billant & Chomaz 2000*a*, *b*) which renders the analysis more intricate. No experimental results of the elliptic instability in a cylinder are available in the presence of stratification.

This paper is based on the PhD thesis of Guimbard (2008). It mainly follows the study already performed in Le Bars *et al.* (2007) without stratification. In § 2, the theory of the elliptic instability in the presence of stratification and background rotation in a cylinder is presented. The mechanism of instability is shortly reviewed and a general explicit formula for the growth rate of the helical instability modes is provided including viscous and detuning effects. In § 3, experimental results are obtained and compared to the theory. A good agreement for the instability threshold is demonstrated. The main results are discussed and summarized in the last section.

2. Theory

2.1. *Base flow*

We consider an incompressible viscous fluid of kinematic viscosity ν in a rotating cylinder of radius R^* and height H^*. The fluid is stably stratified along the cylinder axis with a constant Brunt–Väisälä frequency N^*. The vertical boundary of the cylinder is elliptically deformed with small and large diameters $2R_m^*$ and $2R_M^*$, respectively, and the ellipse is assumed to be stationary in a frame rotating at the angular velocity Ω_t.

In this rotating frame, the fluid in the cylinder is assumed to rotate at the angular velocity Ω_c. The base flow is thus characterized by five parameters: the aspect ratio H, the eccentricity ε of the ellipse, the normalized absolute vorticity W_a, the normalized Brunt–Väisälä frequency N and the Reynolds number Re which are, respectively, defined by

$$H = H^*/R^*, \tag{2.1a}$$

$$\varepsilon = \frac{(R_M^*)^2 - (R_m^*)^2}{(R_M^*)^2 + (R_m^*)^2}, \tag{2.1b}$$

$$W_a = 2(\Omega_c + \Omega_t)/\Omega_c, \tag{2.1c}$$

$$N = N^*/\Omega_c, \tag{2.1d}$$

$$Re = \Omega_c R^{*2}/\nu. \tag{2.1e}$$

Note that W_a is related to the Rossby number $Ro = \Omega_c/\Omega_t = 1/(W_a - 2)$, and that N can be considered as the inverse of a horizontal Froude number.

If R^* and Ω_c^{-1} are used as characteristic scales to non-dimensionalize all variables, the base-flow stream function can be written in the frame rotating with the strain field as

$$\Psi = -\frac{r^2}{2}(1 - \varepsilon \sin 2\theta), \tag{2.2}$$

where r and θ are the polar coordinates. If we neglect the diffusion of the density and assume that $R^*(\Omega_c + \Omega_t)^2 \ll g$, the above expression defines a two-dimensional velocity field which is a solution of the Navier–Stokes equations under the Boussinesq approximation for all ε and Re. The condition $R^*(\Omega_c + \Omega_t)^2 \ll g$, which is satisfied in the experiments carried out below guarantees that the deformation of the isopycnals remains negligible.

In the following, we shall consider small ε and large Re. In these limits, the weak boundary-layer effects on the boundaries at $z = 0$, H and $r = 1$ can be neglected, and this base flow can, in principle, be approximately reproduced with the apparatus described in § 3. The weak diffusion of the density is neglected throughout the paper.

2.2. *Kelvin modes*

Following the theory already described in Waleffe (1990) and Eloy *et al.* (2003), we first search global-mode perturbations (Kelvin modes) of the undeformed cylinder ($\varepsilon = 0$) in the form

$$(\bar{u}, p, b) = (u_r(r)\cos kz, u_\theta(r)\sin kz, u_z(r)\sin kz, p(r)\cos kz, \rho(r)\sin kz)e^{im\theta - i\omega t}, \tag{2.3}$$

where $\bar{u} = (u_r, u_\theta, u_z)$, p and ρ stand for the velocity, pressure and density perturbation fields, respectively. The slip boundary conditions at $z = 0$, H impose that $k = p\pi/H$ with p an integer; the radial boundary condition writes $u_r(r = 1) = 0$. The linearized Euler equations under the Boussinesq approximation for the velocity, pressure and density of the global mode can be reduced to a single equation for the pressure amplitude:

$$\frac{\mathrm{d}^2 p}{\mathrm{d}r^2} + \frac{1}{r}\frac{\mathrm{d}p}{\mathrm{d}r} + \left(\alpha^2 - \frac{m^2}{r^2}\right) p = 0, \tag{2.4}$$

with a radial wavenumber α given by

$$\alpha = k\sqrt{\frac{W_a^2 - \lambda^2}{\lambda^2 - N^2}}, \tag{2.5}$$

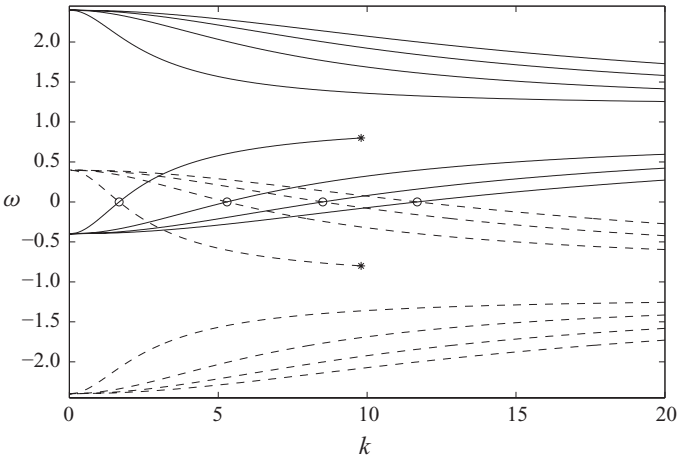

FIGURE 1. Frequency ω versus k of the first four Kelvin modes for $m=1$ (solid lines) and for $m=-1$ (dashed lines) and $W_a=-0.2$ and $N=1.4$. The principal modes $(m_1, m_2, i)=(-1, 1, i)$, $i=1, 2, 3, 4$ are indicated by circles. The first branch stops at a finite wavenumber which is indicated by an asterisk.

where W_a and N have been defined in (2.1*c*, *d*), and $\lambda=\omega-m$ is the inertial frequency of the mode. The solution of (2.4) which is finite on the cylinder axis $r=0$ is $\mathrm{J}_m(\alpha r)$, i.e. the Bessel function of first kind of order m. Applying the boundary condition at $r=1$ to the radial velocity u_r, we can easily deduce the dispersion relation of the mode

$$(\lambda+W_a)\mathrm{J}_{m-1}(\alpha)=(\lambda-W_a)\mathrm{J}_{m+1}(\alpha). \tag{2.6}$$

With α prescribed by (2.5) for each discrete value of k, this equation admits an infinity of solutions for λ which all satisfy $\min(W_a^2, N^2)\leqslant\lambda^2\leqslant\max(W_a^2, N^2)$. This property results from (2.5) which is equivalent to the classical local dispersion relation $\lambda^2=N^2\sin^2\phi+W_a^2\cos^2\phi$ of inertia-gravity waves, where ϕ is the angle of the wavevector $\boldsymbol{k}_{local}=(\alpha, k)$ with respect to the vertical axis. A typical illustration of the dispersion relation is shown in figure 1 for $m=\pm1$. It is worth mentioning that stratification implies a peculiar behaviour of the dispersion relation: as soon as $N^2>W_a^2$, the first upper branch when $W_a>0$ (respectively, the first lower branch when $W_a<0$) stops at a finite wavenumber

$$k_f=\frac{\sqrt{(|m|+1)|m|\left(N^2-W_a^2\right)}}{|W_a|}, \tag{2.7}$$

for which $\lambda^2=W_a^2$ and $\alpha=0$. As we shall see below, this particular branch is responsible for the discrepancy we shall observe between local and global estimates for the inviscid instability growth rate close to $W_a=-1$ for $N>1$.

Viscous effects are expected to damp the neutral inviscid modes. Both boundary-layer and volumic effects are present. The complex viscous correction to the frequency associated with the viscous boundary layers has been calculated by Kudlick (1966) for an unstratified configuration (see also Greenspan 1968; Kerswell & Barenghi 1995). Upon neglecting the diffusion of the density, his calculation can be reproduced in the presence of stratification. For a given mode of axial and azimuthal wavenumbers k and m, the viscous boundary correction to its inviscid frequency ω is found to be

$\delta\omega_S/\sqrt{Re}$, where

$$\delta\omega_S = -G\left[m^2\sqrt{|\lambda|}(i-\mathrm{sgn}(\lambda)) + \frac{k^2\lambda^2}{|\beta|^{3/2}}(i-\mathrm{sgn}(\beta))\right]$$
$$-\frac{G}{H}\left[(i\varepsilon^+-1)\frac{W_a^-}{\sqrt{|W_a^+|}}\left(B-\frac{2m\lambda}{W_a^-}\right)+(i\varepsilon^-+1)\frac{W_a^+}{\sqrt{|W_a^-|}}\left(B-\frac{2m\lambda}{W_a^+}\right)\right], \quad (2.8)$$

with

$$W_a^+ = W_a+\lambda, \quad W_a^- = W_a-\lambda, \varepsilon^\pm = \mathrm{sgn}(W_a^\pm), \quad \beta = \frac{\lambda^2-N^2}{\lambda} \quad (2.9)$$

$$G = \frac{\left(W_a^2-\lambda^2\right)(\lambda^2-N^2)}{\sqrt{2}\lambda^2\left(W_a^2-N^2\right)\left(B-\dfrac{mW_a(\lambda^2-N^2)}{\lambda\left(W_a^2-N^2\right)}\right)}, \quad B = m^2+\frac{k^2\lambda^2}{\lambda^2-N^2} \quad (2.10)$$

and $\mathrm{sgn}(x)$ is equal to 1 for $x>0$ and equal to -1 for $x<0$. The details of the derivation of this formula can be found in Guimbard (2008). The first term in (2.8) is the contribution from the boundary at $r=1$, while the second term is from the boundaries at $z=0, H$. The expression of Kudlick (1966) (see Kerswell & Barenghi 1995) is recovered without background rotation nor stratification ($W_a=2$; $N=0$).

The volumic damping associated with viscous diffusion (density diffusion is neglected) can be computed by a simple asymptotic procedure which has been described in Eloy *et al.* (2003) for instance. We obtain a frequency correction for a mode (k,m,ω) which can be written as $\delta\omega_V/Re$ with

$$\delta\omega_V = -i(\alpha^2+k^2)\left(1-\frac{N^2\left(W_a^2-\lambda^2\right)}{2\lambda^2\left(W_a^2-N^2\right)}\frac{B}{B-\dfrac{mW_a(\lambda^2-N^2)}{\lambda\left(W_a^2-N^2\right)}}\right) \quad (2.11)$$

where B has been defined in (2.10). Note that without stratification this expression is particularly simple, i.e. $\delta\omega_V=-i(\alpha^2+k^2)$ and corresponds to the local estimate $-ik^2_{local}$ (Landman & Saffman 1987). For $W_a=0$, the viscous volumic damping also takes a simple expression which does not depend on the stratification: $\delta\omega_V=-i(\alpha^2+k^2)/2$.

2.3. *Elliptic instability*

The elliptic instability appears when the rotating flow is subject to a strain field. As reviewed by Kerswell (2002), the mechanism of instability can be understood as a triadic resonance of two Kelvin modes with the strain field. If the characteristic of these waves are (k_1,m_1,ω_1) and (k_2,m_2,ω_2) in the frame rotating with the strain field, the condition of resonance reads

$$k_1=k_2, \quad m_2-m_1=2 \quad \text{and} \quad \omega_1=\omega_2. \quad (2.12)$$

In particular, the two modes must satisfy $\lambda_2=\lambda_1+2$. In view of the frequency interval of λ, this is possible only if $N>1$ and $|W_a|<1$ or $N<1$ and $|W_a|>1$.

As explained by Fukumoto (2003), there is also a necessary condition on the wave energy of the modes which must be of opposite sign at resonance for instability. Without viscous effects, if this last condition is satisfied, all the resonant modes are unstable. However, Eloy & Le Dizès (2001) have also demonstrated that the most unstable configurations correspond to modes with similar radial structures. These

configurations have been called 'principal' and are denoted by (m_1, m_2, i), where m_1 and m_2 are the azimuthal wavenumbers of the modes and i is the common index of the branch, that is the ranking number of the zero of (2.6). Among these principal modes, the configurations $(-1, 1, i)$ play a particular role because due to the symmetry of the dispersion relation, their resonant frequency is null and the resonant modes are perfectly in phase. This property explains why they generally possess the largest growth rates.

The inviscid growth rate associated with each resonance can be computed by an asymptotic analysis in the limit of small elliptic deformation $\varepsilon \ll 1$. The detail of this procedure has been provided elsewhere (see Waleffe 1989; Eloy & Le Dizès 2001). Here, we only provide the final results for the principal modes $(-1, 1, i)$ because it takes a particularly simple form which has not been given in the literature. We have obtained for the non-viscous growth rate of the resonant configuration $(-1, 1, i)$ a leading-order expression of the form $\sigma_{nv}\varepsilon$ with

$$\sigma_{nv} = \left| \frac{(N^2-1)(W_a+1)^2\left(\alpha_i^2 + (W_a-1)^2\right)}{4(W_a-1)^2(1+W_a)(N^2+W_a) + 4\left(W_a^2 - N^2\right)\alpha_i^2} \right|, \tag{2.13}$$

where α_i is the ith solution of (2.6) with $|\lambda| = 1$ and $\omega = 0$. The above formula extends the local estimate given in Kerswell (2002) and Leblanc (2003)

$$\sigma_{nv}^{local} = \left| \frac{(N^2-1)(1+W_a)^2}{4\left(N^2 - W_a^2\right)} \right|, \tag{2.14}$$

which is recovered when $\alpha_i \to \infty$, i.e. in the short wavelength limit relevant to the local approach. It also generalizes the formula obtained by Waleffe (1989) without stratification ($N = 0$) nor background rotation ($W_a = 2$):

$$\sigma_{nv}(N = 0, W_a = 2) = \frac{9}{16 + \dfrac{8}{\left(1+\alpha_i^2\right)}}. \tag{2.15}$$

At perfect resonance, the resonant configuration $(-1, 1, i)$ has both its radial wavenumber α_i and its frequency $\omega = 0$ prescribed. For a given cylinder of aspect ratio H, since the axial wavenumber is also prescribed, perfect resonance is thus obtained for particular values of $W_a = W_{a_c}(N)$ for which both (2.5) and (2.6) are satisfied simultaneously. When we depart from the perfect-resonance condition, a frequency detuning between the modes is observed which tends to stabilize the resonant configuration when it becomes too important. A leading-order estimate of this frequency detuning of the form $\delta\omega_d \delta W_a$ can be obtained for the configuration $(-1, 1, i)$ when W_a is at δW_a from the resonant absolute vorticity W_{a_c}:

$$\delta\omega_d = \frac{k^2 W_{a_c} + (1-N^2)(W_{a_c}-1)}{\alpha_i^2 + k^2 + W_{a_c}^2 - N^2 - W_{a_c}}. \tag{2.16}$$

If this detuning effect is taken into account together with the viscous effects discussed above, a general explicit formula for the growth rate of the principal mode $(-1, 1, i)$ in a cylinder of aspect ratio H is obtained:

$$\sigma = \sqrt{\sigma_{nv}^2\varepsilon^2 - \left(\frac{\mathrm{Re}(\delta\omega_S)}{\sqrt{Re}} + \delta\omega_d \delta W_a\right)^2} + \frac{\mathrm{Im}(\delta\omega_S)}{\sqrt{Re}} - i\frac{\delta\omega_V}{Re}, \tag{2.17}$$

where $\mathrm{Re}(\delta\omega_S)$ and $\mathrm{Im}(\delta\omega_S)$ denote the real and imaginary parts of $\delta\omega_S$.

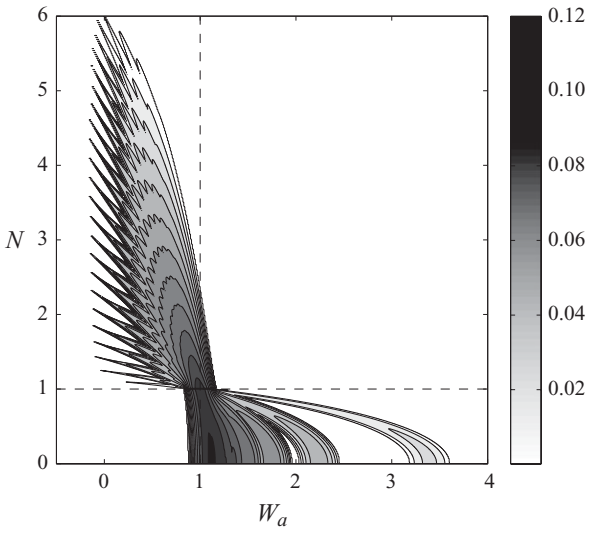

FIGURE 2. Contours of the maximum normalized growth rate σ/ε of modes $(m_1, m_2, i) = (-1, 1, 1)$ for $Re = 1000$, $\varepsilon = 0.179$ and $H = 6.91$. For these parameters, the flow is stable for $W_a < -1$ and $N > 1$ (see also figure 3). This is no longer the case for larger Reynolds numbers (see figure 4).

The contour levels of this expression normalized by ε for the first modes $(-1, 1, 1)$ are plotted in figure 2 for parameters relevant for the experiments discussed in the next section. Note, however, that in the experiments, the parameter N cannot be varied independently of the Reynolds number. Sections of the plot of figure 2 for a weakly stratified case ($N = 1/2$) and a strongly stratified case ($N = 3/2$) are also shown in figures 3(a) and 3(b), respectively. These figures first show that the inviscid domain of instability does correspond to the domain of resonance of the mode: the flow is unstable for $|W_a| > 1$ when $N < 1$ and for $-1 < W_a < 1$ when $N > 1$, in agreement with the local theory (Leblanc 2003). However, the instability domain slightly extends below $W_a = 1$ for $N < 1$ (see figure 3a) and above $W_a = 1$ for $N > 1$ (see figure 3b) due to the finite value of ε. The domain of instability has also a limited extent in both N and W_a directions due to viscous and finite-size effects. For $N < 1$, there is a finite W_a above which the flow becomes stable because as W_a increases the smallest resonant axial wavenumber decreases and the mode no longer fits in the cylinder above a critical W_a. For $|W_a| < 1$, there is a finite N above which the flow becomes stable, because mode $(-1, 1, 1)$, which radially fits in the cylinder, has an axial wavenumber which increases with N: it is therefore more and more affected by viscosity as N increases. This stabilizing effect becomes dominant above a critical N. The 'peaky' structure visible in figure 2 close to $W_a = 0$ is not a numerical artifact. It corresponds to jumps from an axial wavenumber to another. The axial wavenumber of the most unstable mode progressively increases as N increases, until viscous effects become too important for instability. For the parameters of figure 2, the upper critical N is $N_c \approx 6$ for the wavenumber $k_c = 24\pi/H$.

In figure 3 is also plotted the normalized growth rate of the second mode $(-1, 1, 2)$. For this Reynolds number $Re = 1000$, only the first two principal modes $(-1, 1, i)$ with $i = 1, 2$ are unstable and no unstable modes exist for negative W_a when $N = 1/2$. We have to consider much larger values of Reynolds number to be able to obtain unstable modes for $W_a < -1$. These unstable modes are visible in figure 4 where we

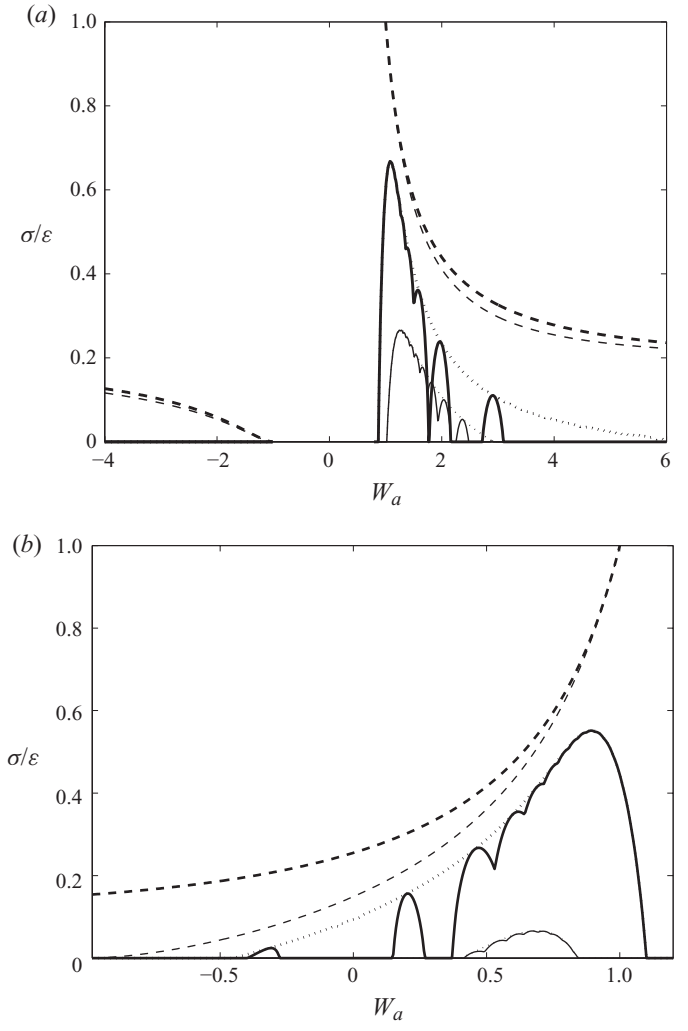

FIGURE 3. Normalized growth rate of the resonant configurations $(-1, 1, 1)$ (thick lines) and $(-1, 1, 2)$ (thin lines) for (a) $N = 1/2$ and (b) $N = 3/2$ and for $Re = 1000$ and $\varepsilon = 0.179$. Viscous formula (see (2.17)) for $H = 6.91$ (solid line) and $H = \infty$ (dotted line) and non-viscous formula (see (2.13)) for $H = \infty$ (dashed line). One can notice that the viscous corrections significantly decrease the growth rate of the instability, whereas the finite value of H induces a discretization of the resonance bands, each band corresponding to a given axial wavenumber.

have plotted the same growth-rate curves, as shown in figure 3(a), but for $Re = 10\,000$. We have not been able to consider such high Reynolds numbers with $W_a < -1$ in the experiments.

It is interesting to point out the important difference between the inviscid estimates for the first two modes in figure 3(b) for $N = 3/2$ close to $W_a = -1$. The first mode is expected to be inviscidly unstable close to $W_a = -1$, while the second mode, and all the higher order modes are neutrally stable, in agreement with the local estimate (2.14). This difference is linked to the peculiar property of the first branch which has been mentioned above. As $W_a \to -1$, the characteristics of the principal $(-1, 1, i)$ are such that α_1 goes to zero, while all the other $\alpha_i, i > 1$ go to infinity as in the local approach.

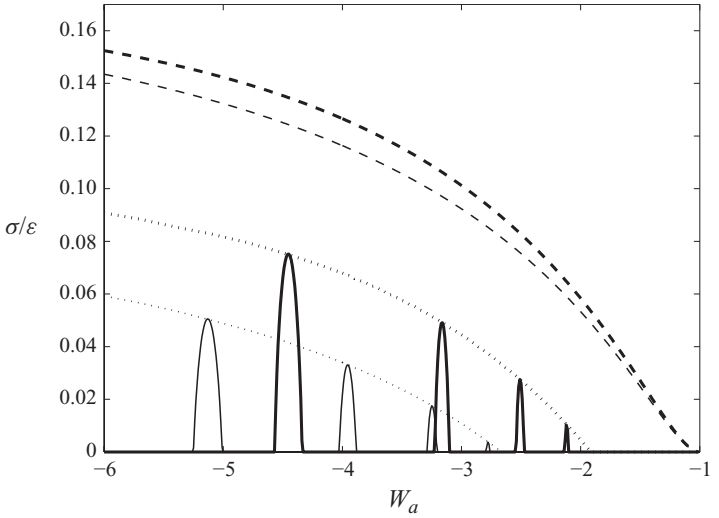

FIGURE 4. Same as figure 3(*a*) for $Re = 10\,000$. Zoom on the $W_a < -1$ region.

3. Experiments

The purpose of our experimental study is twofold: first, we want to test the various conclusions of the theoretical study, in particular the threshold of instability in the case of small and large stratifications as well as the characteristics of the excited mode (growth rate and wavelength); and second, we want to complete this theoretical study by observing the nonlinear evolution of the instability.

3.1. *Experimental set-up*

Our experimental set-up is similar to the one presented in Le Bars *et al.* (2007): a deformable and transparent plastic cylinder of radius 2.75 cm and height 19.0 cm (which gives $H = 6.91$) is set in motion about its axis (Oz) with an angular velocity Ω_c up to 7.3 rad s^{-1}, and is simultaneously deformed elliptically by two fixed rollers parallel to (Oz). Deformations of eccentricity $\varepsilon = 0.085$ and $\varepsilon = 0.179$ have been considered. The container is filled with a solution of salted water with a linear stratification along the rotation axis (Oz), realized with the classical two-tank method (e.g. see Hill 2002). Constant Brunt–Väisälä frequencies N^* are obtained in the range 2.7–3.4 rad s^{-1} with a precision of about 5 %. For visualization, the salted water is seeded with anisotropic particles (Kalliroscope) and a vertical light sheet is formed in a plane containing the rotation axis and the principal axis of the straining field, allowing the measurement of wavelengths and frequencies of excited modes. The whole set-up is finally placed on a 0.5 m diameter rotating table, with angular velocity Ω_t up to ± 2 rad s^{-1}. Our protocol is the same all along the experiments presented here. Once the stratification is established, the table rotation and the cylinder rotation are simultaneously set to their initial assigned value: a spin-up phase first takes place, before the possible development of an instability. Once either stability or instability is clearly observed (i.e. typically after several minutes), the table angular velocity and/or the cylinder angular velocity are changed in order to explore a large range in N and W_a. The duration of an experiment is limited by the resistance of the plastic cylinder, which is submitted to a strong deformation and typically breaks after 30 min. Note that since N^* does not significantly change in our experiments,

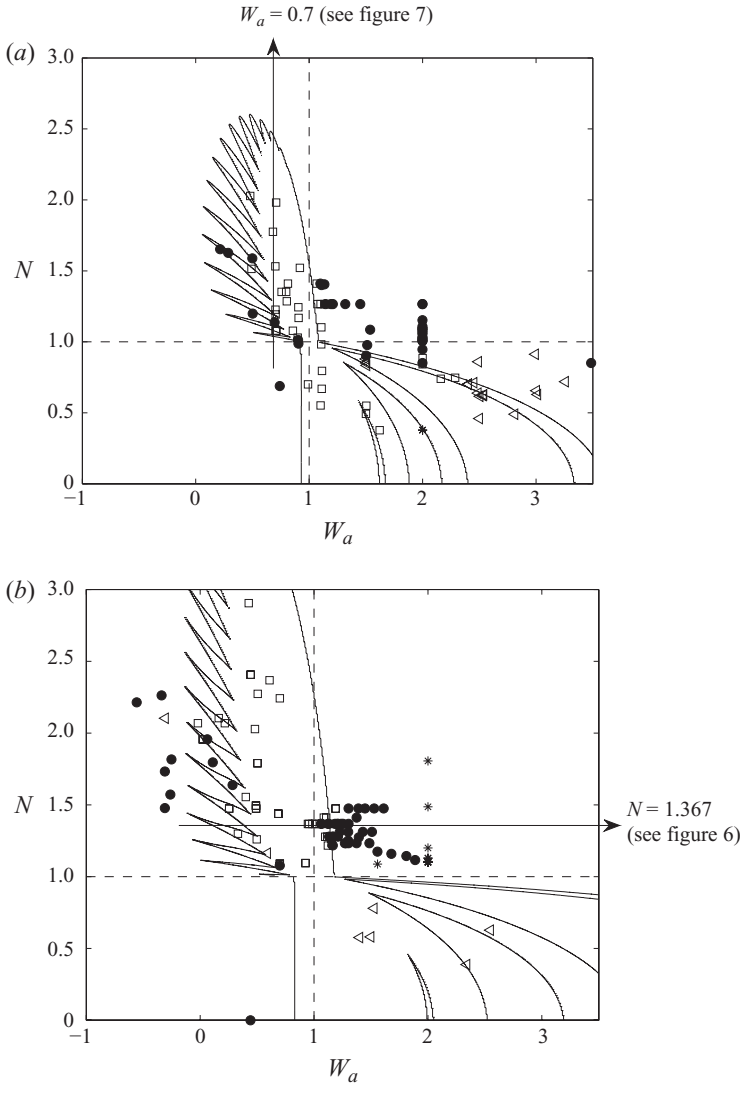

FIGURE 5. Regime diagram for all performed experiments with $H = 6.91$ and $N^* \in [2.7; 3.4]$ rad s^{-1}. (*a*) $\varepsilon = 0.085$ and (*b*) $\varepsilon = 0.179$. Each symbol represents an experiment with the following characteristics. Black circles: stable; open squares: mode $(-1, 1)$; open triangles: mode $(0, 2)$; asterisks: centrifugal mode. The solid line indicates the theoretical instability diagram for modes $(-1, 1, 1)$ with $Re = 2100/N$, corresponding to a constant $N^* = 3$ rad s^{-1}. The horizontal and vertical arrows indicate the location of series of experiments performed at a constant N and a constant W_a, which are shown in figures 6 and 7, respectively.

variations in N are mostly related to changes in the cylinder angular velocity Ω_c. This also implies that the Reynolds number is approximately inversely proportional to N, i.e. $Re = (N^* R^{*2}/\nu)/N$.

3.2. *Determination of the threshold of instability*

All performed experiments are presented in figure 5, where the observed regime is plotted as a function of the absolute vorticity W_a and the dimensionless Brunt–Väisälä frequency N. The Reynolds number is not constant in these plots. The

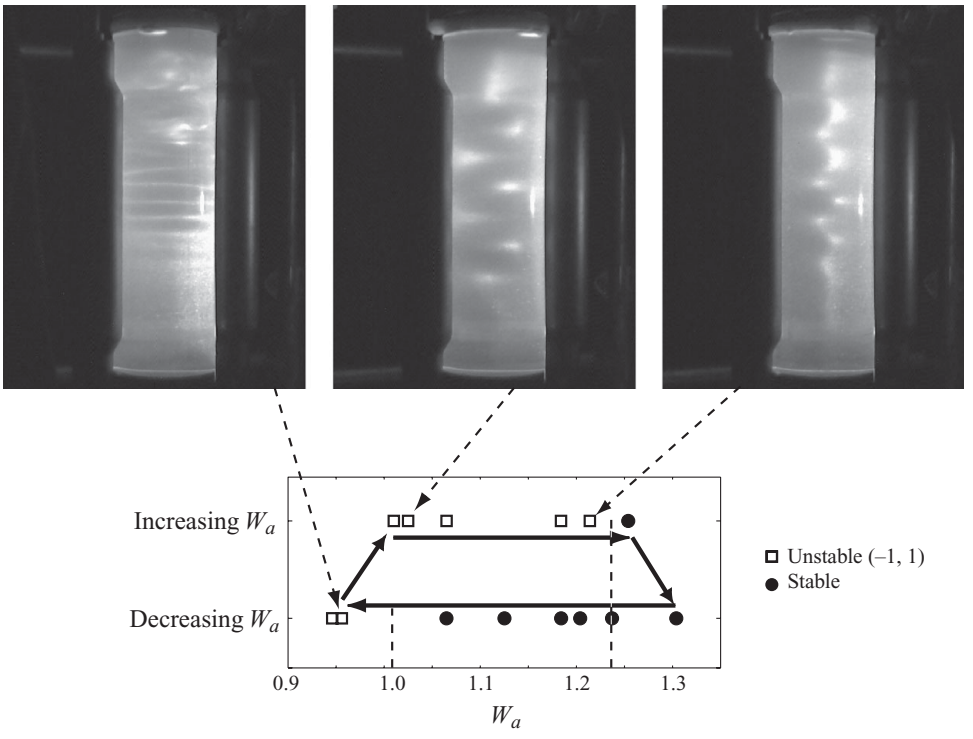

FIGURE 6. Series of experiments performed at constant values of $\varepsilon = 0.179$, $Re = 1.5 \times 10^3$, $N = 1.367$ and for various values of the absolute vorticity, illustrating the hysteresis of the instability threshold. The thick arrows indicate the experimental protocol, first starting from the stable domain at large W_a and decreasing it until the appearance of the instability, then increasing W_a until the disappearance of the instability, and finally decreasing W_a again. Images illustrate the excited mode, with a shorter wavelength close to thresholds in agreement with the theoretical predictions.

theoretical instability domain for modes $(-1, 1, 1)$ has been indicated in solid line for a Reynolds number given by $Re = 2100/N$ which corresponds to a Brunt–Väisälä frequency $N^* = 3$ rad s^{-1}. A first look at this figure shows a general agreement with the analytical conclusions: instability is mainly observed either for large absolute vorticity and small stratification (i.e. $W_a > 1$ and $N < 1$) or for small absolute vorticity and large stratification (i.e. $|W_a| < 1$ and $N > 1$). The experiments are in very good agreement with the theory for modes $(-1, 1, 1)$: all the observations of the modes $(-1, 1, 1)$ fell within (or are very close to) the theoretical instability domain of these modes. Note, in particular, that the small instability band obtained close to $W_a = 2$ and $N = 0.8$ is captured by the experiments for $\varepsilon = 0.085$ (see figure 5*a*).

Unfortunately, our set-up does not allow to explore the $W_a < -1$ parameter space, where instability is also expected for weak stratification and large Reynolds numbers (see figure 4).

A closer look at figure 5, however, exhibits some overlapping between stable and unstable experiments around the lines $W_a = 1$ and $N = 1$. This is due to the experimental procedure, and more precisely to the way that the assigned values of W_a and N are reached, as illustrated in figure 6. When starting from a stable situation and progressively decreasing W_a (for instance) to reach the unstable regime, an excellent agreement is found between the theory and the experiment. However, once the flow is

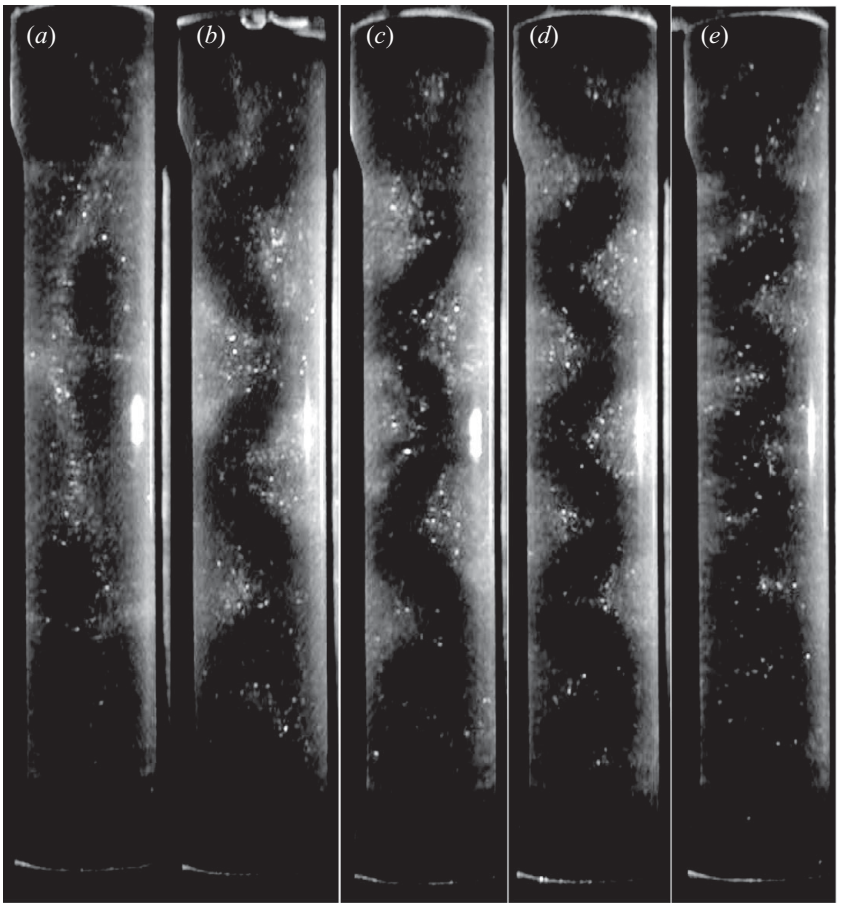

FIGURE 7. Series of experiments performed at constant values of $\varepsilon = 0.085$, $W_a = 0.70$ and $N^* = 2.68$ rad s^{-1}, systematically changing Ω_c and Ω_t to illustrate the influence of N on the wavelength selection. (*a*) $N = 1.08$, (*b*) $N = 1.35$, (*c*) $N = 1.53$, (*d*) $N = 1.77$ and (*e*) $N = 1.98$.

destabilized, re-increasing W_a does not lead immediately to re-stabilization, suggesting a subcritical instability.

3.3. *Mode selection*

As predicted by the theory, the most unstable mode over almost all the domain corresponds to the stationary mode $(-1, 1, 1)$, experimentally characterized by a sinusoidal rotation axis. The axial wavenumber of the most unstable mode, however, depends on N and W_a. Figure 7 illustrates the variation of the axial wavenumber with respect to N for a fixed $W_a < 1$. One observes the general trend already mentioned above that the axial wavenumber increases as N increases. The measured axial wavenumber is compared to the theory in figure 8. We can see that, for this value of W_a, there is a very good agreement between the theory and the experiments. Discrepancies between the theoretical and the experimental wavelengths may appear either for very large wavelengths, where finite-size effects of our experimental cylinder are especially important and may lead to the selection of a smaller wavelength as expected, or for very small wavelengths, where various resonances are close and

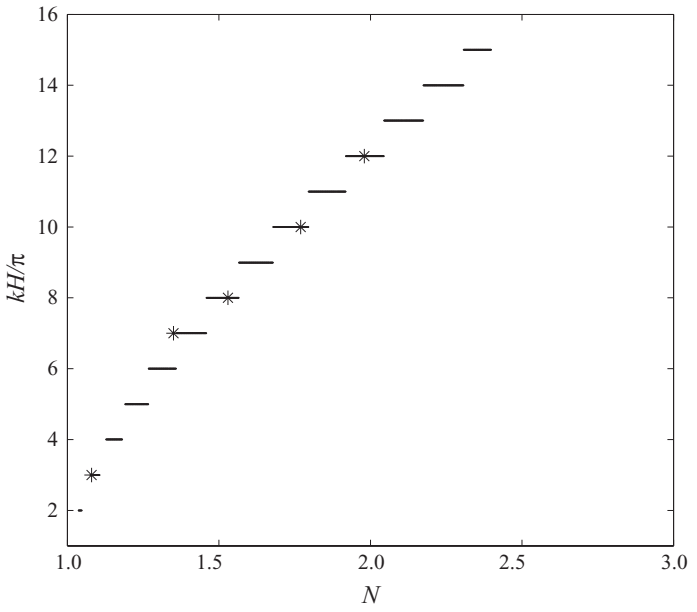

FIGURE 8. Most unstable wavenumber predicted by the theory for the parameters of figure 7, together with the experimental measurements indicated by asterisks.

diffusive effects are especially important, which may lead to the selection of a larger wavelength as expected.

Mode $(-1, 1, 1)$ is interesting from an experimental point of view, because its growth rate can be easily determined from our Kalliroscope visualization: from sequences of images, we measure the maximum amplitude of the sinusoidally deformed rotation axis; its temporal evolution is then fitted with an exponential growth, which can be compared to the exponential growth rate determined analytically. Typical space–time diagrams are shown in figure 9. For the two cases considered in this figure, the exponential growth rates $\sigma/\varepsilon \approx 0.43$ and $\sigma/\varepsilon \approx 0.28$ are fairly in good agreement with the theoretical predictions $\sigma/\varepsilon \approx 0.65$ and $\sigma/\varepsilon \approx 0.28$, respectively.

Finally, note that a mode $(0, 2, 1)$ characterized by a pulsating behaviour with a period $2\pi/\Omega_c$ is observed in certain regions of the parameter space where a mode $(-1, 1, 1)$ could *a priori* also exist (see figure 5*b* for $W_a > 1$ and $N < 1$). In these regions, we suspect that the growth rate of modes $(0, 2, 1)$ is larger than that of modes $(-1, 1, 1)$. Mode $(0, 2, 1)$ can also be present in regions where modes $(-1, 1, 1)$ are all stable (see figure 5*a* for $W_a > 2.5$). This is a finite-size effect which was also observed in the absence of stratification (Le Bars *et al.* 2007): the theoretical wavelength of the first mode $(-1, 1, 1)$ is too large to fit within the container.

3.4. *Nonlinear behaviour*

As demonstrated in the previous section, experiments in the unstable regime first exhibit an exponential growth of the perturbations in agreement with the linear theory. Then, the instability mode either saturates when the Reynolds number is very close to threshold, or evolves towards a turbulent state at slightly larger Reynolds numbers, as illustrated in the space–time diagram of figure 9(*a*). For the strongly stratified cases ($N > 1$), this turbulent state persists in contrast with experiments without stratification where a cyclic behaviour with growth, breakdown and re-laminarization takes place

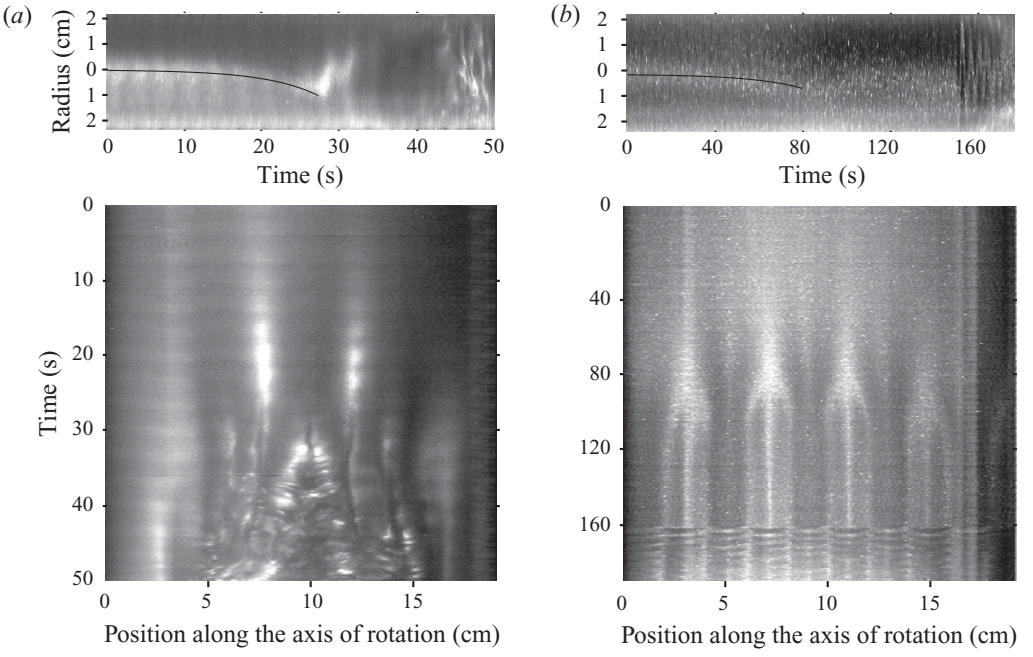

FIGURE 9. Spatio-temporal diagrams obtained by extracting the same line perpendicular (upper images) or parallel (lower images) to the rotation axis in each image of a given video sequence. (*a*) $\varepsilon = 0.179$, $Re = 1.5 \times 10^3$, $N = 1.367$ and $W_a = 0.946$ and (*b*) $\varepsilon = 0.085$, $Re = 1.1 \times 10^3$, $N = 1.775$ and $W_a = 0.680$. Lines on the upper images indicate the exponential growth of the excited mode with an experimentally determined growth rate $\sigma/\varepsilon = 0.43$ and $\sigma/\varepsilon = 0.28$, respectively, in good agreement with theoretical predictions, i.e. $\sigma/\varepsilon = 0.65$ and $\sigma/\varepsilon = 0.28$.

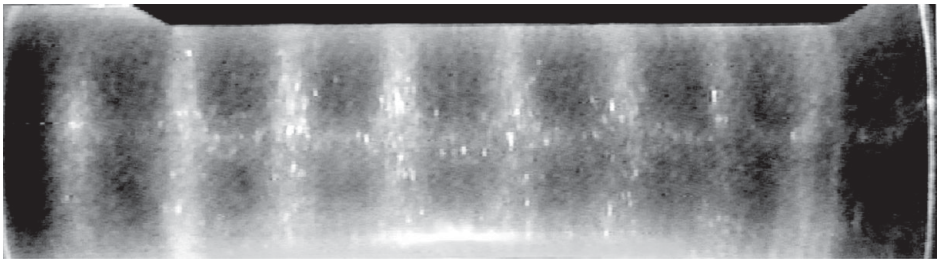

FIGURE 10. Centrifugal instability observed during the spin-up phase for $\varepsilon = 0.179$, $W_a = 2.0$, $N = 1.2$ and $Re = 1.9 \times 10^3$. In this figure, the direction of gravity and the axis of rotation are horizontal.

(e.g. see Eloy *et al.* 2003). We think that the absence of re-laminarization is due to the strong stratification which prevents the development of an efficient Ekman pumping. Note, however, that in some cases, an intermediate scenario between saturation and turbulence with a wavenumber doubling is observed, as illustrated in figure 9(*b*).

Another nonlinear effect is the presence of a new type of instability, as illustrated in figure 10 and labelled with asterisks in figure 5. This instability appears during the spin-up phase, and is stationary and symmetric about the axis of rotation. We do not expect it to be related to the elliptic instability, whose unique stationary modes are the modes $(-1, 1)$, which are antisymmetric about the axis of rotation. Moreover, we have not observed this instability in the regime where the modes $(-1, 1)$ were

unstable. The present instability clearly looks like a centrifugal mode. We suspect that it appears because the base-flow corrections generated by the elliptic deformation of the boundary make the flow centrifugally unstable during the spin-up phase. This point is clearly not taken into account in our theory, where we start from an already established base flow with constant eccentricity and constant vorticity. It will be the subject of a forthcoming experimental and theoretical study. Note, however, that this centrifugal instability is not expected to be associated with the stratification. Such an instability was indeed already observed by Eloy (2000) without stratification in large Reynolds numbers experiments when a spin-up phase was present. In these cases, the centrifugal mode was typically observed to grow, breakdown and totally disappear after the first re-laminarization, thus demonstrating its relation with the spin-up phase. In the present case, however, stratification considerably reduces any large-scale recirculation along the axis of stratification, hence the re-laminarization: once excited, the centrifugal mode persists over the duration of the experiment.

To finish with, note that this last point clearly illustrates the main difficulty in comparing theoretical and experimental results: starting from a fluid at rest, we have no insurance to converge towards the base flow expected theoretically, i.e. a uniform elliptical flow. This is especially true for experiments with zero absolute vorticity, for which the theoretical spin-up time goes towards infinity. This could perhaps explain why we have not succeeded in observing the elliptic instability close to $W_a = 0$ for a configuration starting from rest. In fact, we only observed the instability for zero absolute vorticity with the relevant wavelength when first generating a turbulent motion before suddenly adjusting simultaneously the table and cylinder rotations to opposite values. This again demonstrates the influence of the experimental protocol. We think that a more detailed analysis of the transient in the presence of elliptic deformation is crucially needed to clarify this point.

4. Conclusion

In this paper, we have analysed the effects of background rotation and stratification on the elliptic instability in a cylinder. A general formula for the growth rate of the principal modes $(-1, 1, i)$ has been obtained which extends the previous formulae given in the literature. This formula, which has been obtained by performing an asymptotic analysis for small eccentricity and large Reynolds numbers, includes the effect of the finite size of the cylinder and the boundary and volumic viscous effects. We have shown that these finite-size and viscous effects are responsible for the existence of a critical Brunt–Väisälä frequency and a critical absolute vorticity $|W_a|$ above which the flow becomes stable.

Experimental results have been obtained by using a stratified fluid (salted water) in an elliptically deformed rotating cylinder placed on a rotating table. A large range of parameters has been explored by varying the angular velocity of both the cylinder and the table. The principal modes $(-1, 1, 1)$ have been visualized in large regions of the parameter space where the mode was expected to be unstable from the theory. A difficult measure of the growth rate of these modes has been performed for two different cases and found to be in reasonable agreement with the theoretical prediction. Other regimes have also been observed. Mode $(0, 2, 1)$, which oscillates at the rotation frequency of the cylinder has been obtained for certain parameters for which modes $(-1, 1, 1)$ were stable or less unstable. A new instability, which resembles a centrifugal instability has also been evidenced in regimes where the flow was expected to be stable with respect to the elliptic instability. This instability, which

deserves a complete study, seems to be associated with the spin-up phase which is present in the experiment.

Some informations on the nonlinear evolution of the elliptic instability have also been provided. We have seen that the elliptic instability, in general, leads to a turbulent regime which persists. No re-laminarization process has been observed contrarily to what was observed in an homogeneous fluid (Eloy *et al.* 2003).

As mentioned in § 1, the results obtained here are expected to apply qualitatively to vortices with steep vorticity profiles. For these vortices, critical-point singularities are not expected to damp the Kelvin modes (Schecter & Montgomery 2004) and therefore the conditions of resonance of the Kelvin modes are expected to remain similar. However, for a vortex, like the Lamb–Oseen vortex which has a Gaussian vorticity profile, critical-point singularities are known strongly to affect the characteristics of the Kelvin modes (Le Dizès & Lacaze 2005; Fabre, Sipp & Jacquin 2006). As a consequence, the condition of resonance could be modified and instability could disappear. Le Dizès (2008) has analysed how the domain of the elliptic instability is expected to be modified by this effect for strongly and weakly stratified fluids for a Lamb–Oseen vortex. The presence of a critical point could also have a destabilizing effect. Le Dizès & Billant (2009) have shown that this peculiar behaviour is associated with internal wave emission. It could explain the spontaneous destabilization of a single Lamb–Oseen vortex without the need of strain fields (Riedinger, Le Dizès & Meunier 2010). The coupling between Kelvin modes and internal waves is also at the origin of the so-called strato-rotational instability which occurs in the finite geometry of a Taylor–Couette system (Molemaker, McWilliams & Yavneh 2001; Le Bars & Le Gal 2007).

Financial supports from the French Ministry of Research under the grant "ACI Jeunes chercheurs" (D. G. and S. L.) and from the French National Research Agency (ANR) under the grant ANR-07BLAN-0182 (S. L. D., M. L. B. and P. L. G.) are acknowledged. We are also grateful to Paul Billant for stimulating discussions.

REFERENCES

Bayly, B. J. 1986 Three-dimensional instability of elliptical flow. *Phys. Rev. Lett.* **57**, 2160–2163.

Bayly, B. J., Orszag, S. A. & Herbert, T. 1988 Instability mechanisms in shear-flow transition. *Annu. Rev. Fluid Mech.* **20**, 359–391.

Billant, P. & Chomaz, J.-M. 2000*a* Theoretical analysis of the zigzag instability of a columnar vortex pair in a strongly stratified fluid. *J. Fluid Mech.* **419**, 29–63.

Billant, P. & Chomaz, J.-M. 2000*b* Three-dimensional stability of a vertical columnar vortex pair in a stratified fluid. *J. Fluid Mech.* **419**, 65–91.

Billant, P., Colette, A. & Chomaz, J.-M. 2004 Instabilities of a vortex pair in a stratified and rotating fluid. In *XXI International Congress of Theoretical and Applied Mechanics, 15–21 August 2004*, Warsaw, Poland. CD Rom.

Cariteau, B. & Flór, J.-B. 2006 An experimental investigation on elliptical instability of a strongly asymmetric vortex pair in a stable density stratification. *Nonlinear Process. Geophys.* **13**, 641–649.

Eloy, C. 2000 Instabilité multipolaire de tourbillons. PhD thesis, Université Aix-Marseille II, Marseille, France.

Eloy, C. & Le Dizès, S. 2001 Stability of the Rankine vortex in a multipolar strain field. *Phys. Fluids* **13** (3), 660–676.

Eloy, C., Le Gal, P. & Le Dizès, S. 2000 Experimental study of the multipolar vortex instability. *Phys. Rev. Lett.* **85** (16), 145–166.

Eloy, C., Le Gal, P. & Le Dizès, S. 2003 Elliptic and triangular instabilities in rotating cylinders. *J. Fluid Mech.* **476**, 357–388.

Etling, D. 1989 On atmospheric vortex streets in the wake of large islands. *Meteorol. Atmos. Phys.* **41**, 157–164.

Fabre, D., Sipp, D. & Jacquin, L. 2006 The Kelvin waves and the singular modes of the Lamb–Oseen vortex. *J. Fluid Mech.* **551**, 235–274.

Fukumoto, Y. 2003 The three-dimensional instability of a strained vortex tube revisited. *J. Fluid Mech.* **493**, 287–318.

Greenspan, H. P. 1968 *The Theory of Rotating Fluids*. Cambridge University Press.

Guimbard, D. 2008 L'instabilité elliptique en milieu stratifié tournant. PhD thesis, Université de Toulon et du Var, Toulon, France.

Hill, D. F. 2002 General density gradients in general domains: the "two-tank" method revisited. *Exp. Fluids* **32**, 434–440.

Kerswell, R. 1993 Elliptical instabilities of stratified, hydromagnetic waves. *Geophys. Astrophys. Fluid Dyn.* **71**, 105–143.

Kerswell, R. R. 2002 Elliptical instability. *Annu. Rev. Fluid Mech.* **34**, 83–113.

Kerswell, R. R. & Barenghi, C. F. 1995 On the viscous decay rates of inertial waves in a rotating circular cylinder. *J. Fluid Mech.* **285**, 203–214.

Kudlick, M. 1966 On the transient motions in a contained rotating fluid. PhD thesis, MIT, Cambridge, MA.

Landman, M. J. & Saffman, P. G. 1987 The three-dimensional instability of strained vortices in a viscous fluid. *Phys. Fluids* **30** (8), 2339–2342.

Le Bars, M., Le Dizès, S. & Le Gal, P. 2007 Coriolis effects on the elliptical instability in cylindrical and spherical rotating containers. *J. Fluid Mech.* **585**, 323–342.

Le Bars, M. & Le Gal, P. 2007 Experimental analysis of the stratorotational instability in a cylindrical Couette flow. *Phys. Rev. Lett.* **99**, 064502.

Le Dizès, S. 2008 Inviscid waves on a Lamb–Oseen vortex in a rotating stratified fluid: consequences on the elliptic instability. *J. Fluid Mech.* **597**, 283–303.

Le Dizès, S. & Billant, P. 2009 Radiative instability in stratified vortices. *Phys. Fluids* **21**, 096602.

Le Dizès, S. & Lacaze, L. 2005 An asymptotic description of vortex Kelvin modes. *J. Fluid Mech.* **542**, 69–96.

Leblanc, S. 2003 Internal wave resonances in strain flows. *J. Fluid Mech.* **477**, 259–283.

Lesieur, M., Métais, O. & Garnier, E. 2000 Baroclinic instability and severe storms. *J. Turb.* **1**, 1–17.

Leweke, T. & Williamson, C. H. K. 1998 Three-dimensional instabilities in wake transition. *Eur. J Mech.* B/*Fluids* **17**, 571–586.

Lifschitz, A. & Hameiri, E. 1991 Local stability conditions in fluid dynamics. *Phys. Fluids* A **3** (11), 2644–2651.

Malkus, W. V. R. 1989 An experimental study of global instabilities due to tidal (elliptical) distortion of a rotating elastic cylinder. *Geophys. Astrophys. Fluid Dyn.* **48**, 123–134.

Miyazaki, T. 1993 Elliptical instability in a stably stratified rotating fluid. *Phys. Fluids* A **5** (11), 2702–2709.

Miyazaki, T. & Fukumoto, Y. 1992 Three-dimensional instability of strained vortices in stably stratified fluid. *Phys. Fluids* A **4**, 2515–2522.

Molemaker, M. J., McWilliams, J. C. & Yavneh, I. 2001 Instability and equilibration of centrifugally stable stratified Taylor–Couette flow. *Phys. Rev. Lett.* **86**, 5270–5273.

Polavarapu, S. M. & Peltier, W. R. 1993 Formation of small-scale cyclones in numerical simulations of synoptic-scale baroclinic wave life cycles: secondary instability at the cusp. *J. Atmos. Sci.* **50**, 1047–1057.

Riedinger, X., Le Dizès, S. & Meunier, P. 2010 Viscous stability properties of a Lamb–Oseen vortex in a stratified fluid. *J. Fluid Mech.* **645**, 255–278.

Schecter, D. A. & Montgomery, M. T. 2004 Damping and pumping of a vortex Rossby wave in a monotonic cyclone: critical layer stirring versus inertia–buoyancy wave emission. *Phys. Fluids* **16**, 1334–48.

Stegner, A., Pichon, T. & Beunier, M. 2005 Elliptical-inertial instability of rotating Karman streets. *Phys. Fluids* **17**, 066602.

Waleffe, F. 1989 The 3D instability of a strained vortex and its relation to turbulence. PhD thesis, Massachusetts Institute of Technology, Cambridge, MA.

Waleffe, F. 1990 On the three-dimensional instability of strained vortices. *Phys. Fluids* A **2** (1), 76–80.